

RIS-Enabled NLoS Near-Field Joint Position and Velocity Estimation under User Mobility

Moustafa Rahal, *Student Member, IEEE*, Benoit Denis, *Member, IEEE*, Musa Furkan Keskin, *Member, IEEE*, Bernard Uguen, *Senior Member, IEEE*, and Henk Wymeersch, *Senior Member, IEEE*

Abstract—In the context of single-base station (BS) non-line-of-sight (NLoS) single-epoch localization with the aid of a reflective reconfigurable intelligent surface (RIS), this paper introduces a novel three-step algorithm that jointly estimates the position and velocity of a mobile user equipment (UE), while compensating for the Doppler effects observed in near-field (NF) at the RIS elements over the short transmission duration of a sequence of downlink (DL) pilot symbols. First, a low-complexity initialization procedure is proposed, relying in part on far-field (FF) approximation and a static user assumption. Then, an alternating optimization procedure is designed to iteratively refine the velocity and position estimates, as well as the channel gain. The refinement routines leverage small angle approximations and the linearization of the RIS response, accounting for both NF and mobility effects. We evaluate the performance of the proposed algorithm through extensive simulations under diverse operating conditions with regard to signal-to-noise ratio (SNR), UE mobility, uncontrolled multipath and RIS-UE distance. Our results reveal remarkable performance improvements over the state-of-the-art (SoTA) mobility-agnostic benchmark algorithm, while indicating convergence of the proposed algorithm to respective theoretical bounds on position and velocity estimation.

I. INTRODUCTION

As the fifth-generation (5G) wireless communication systems are revolutionizing the way we connect and communicate, the industry is now gearing up for the next leap in wireless technology, namely sixth-generation (6G). As we set our sights on this new frontier, a new set of challenges, key performance indicators (KPIs), and enabling technologies are emerging [1]. The vision for 6G encompasses even higher data rates, ultra-reliable and low-latency communication, ubiquitous connectivity, and intelligent network infrastructure to support diverse applications such as autonomous systems, virtual reality, and Internet-of-Things (IoT) [2]–[4]. Meeting these ambitious goals requires breakthroughs in various enabling technologies, including advanced antenna systems, efficient spectrum utilization, edge computing, and innovative signal processing techniques [5]–[7].

This work was supported by the Swedish Research Council (VR grant 2022-03007), by the European Commission through the H2020 project RISE-6G (grant agreement no. 101017011) and Horizon Europe SNS-JU project 6G-BRICKS (grant agreement no. 101096954).

Moustafa Rahal and Benoit Denis are with Université Grenoble Alpes, CEA-Leti, F-38000 Grenoble, France (e-mails: {moustafa.rahal, benoit.denis}@cea.fr).

Musa Furkan Keskin and Henk Wymeersch are with the Department of Electrical Engineering, Chalmers University of Technology, 41258 Göteborg, Sweden (e-mails: {furkan, henkw}@chalmers.se).

Bernard Uguen is with the Université Rennes 1, IETR - UMR 6164, F-35000 Rennes, France (e-mail: bernard.uguen@univ-rennes.fr).

Among the promising enabling technologies for the realization of 6G, reconfigurable intelligent surfaces (RISs) have emerged as a disruptive and transformative concept [8]. RISs, also known as intelligent reflecting surfaces or programmable metasurfaces, are planar structures comprising numerous passive elements that can control and manipulate electromagnetic waves [9]. By dynamically adjusting the phase, the polarization, and even possibly the amplitude, of the incident signals, RISs can actively shape the wireless propagation environment [10]. This ability opens up a myriad of possibilities to enhance the performance and efficiency of wireless systems. RISs can indeed contribute to optimizing signal quality, improve coverage, mitigate interference, and extend the reach of wireless networks, offering a cost-effective, energy-efficient, easy-to-deploy, and scalable solution compared to conventional approaches [11]. The integration of RIS into the wireless ecosystem holds great potential for changing the way we design, deploy, and operate future communication networks, making it a subject of significant research interest and exploration [12]–[17].

In addition to its impact on communication performance, the RIS technology also holds great potential for localization applications [18]. The capability to precisely position user equipments (UEs) in wireless networks is indeed crucial for various emerging services, such as autonomous navigation, augmented reality, and other location-based services but also for network performance improvement [19], [20]. For instance, by leveraging the controllable element-wise phases distribution of a reflective RIS, it is possible to enhance localization continuity, accuracy, and reliability, or even simply just to make localization feasible, in restrictive scenarios and challenging environments [21]. RISs can overcome harsh propagation conditions (e.g., non-line-of-sight (NLoS)) or limited deployment settings for which conventional systems based on active base stations (BSs) would fail [21], [22]. More generally, they can contribute to optimizing signal strength and quality to better estimate the location-dependent radio parameters required for localization [23]. This natural synergy between RISs and localization techniques opens up new possibilities for high-precision positioning. Related open research challenges are summarized in [18]. As concrete examples, reflective RISs have been considered for parametric multipath-aided static UE positioning in two cases: when the BS-UE direct path is present, namely line-of-sight (LoS) [23]–[27], and when it is blocked, i.e., NLoS [21], [28], [29]. In the former case, the BS and UE have at least two communication links, which facilitates the use of the traditional two-step localization

antenna UE and an M -element reflective RIS, visualized in Fig. 1. The LoS path between the BS and the UE is considered to be blocked, thus localization is made feasible by relying on the RIS-reflected paths and the geometric NF model, as in [21]. In this section, we present the geometric and signal models, followed by the problem formulation.

A. Geometric Model

The 3D positions are all expressed in the same global reference coordinates system, as follows: $\mathbf{p}_b \in \mathbb{R}^{3 \times 1}$ is a vector containing the known BS coordinates, $\mathbf{p}_m \in \mathbb{R}^{3 \times 1}$ is a vector holding the known coordinates of the RIS m -th element where $m \in \{1, \dots, M\}$ and r is the reference element which is the RIS center, in our case. Also, $\mathbf{p} \in \mathbb{R}^{3 \times 1}$ holds the UE's coordinates and is expressed as $[p_x, p_y, p_z]^\top$ in the Cartesian coordinates system or as $[\rho, \theta, \phi]^\top$ in the spherical coordinates system. Fig. 1 illustrates the scenario, its geometry, and the chosen coordinates axes. Moreover, we denote by $\mathbf{v} = [v_x, v_y, v_z]^\top \in \mathbb{R}^{3 \times 1}$ the UE velocity vector, and by $v_m = \mathbf{v}^\top \mathbf{u}_m(\mathbf{p})$ the radial velocities along the m -th RIS element - UE direction. We also define $\mathbf{u}_m(\mathbf{p}) = (\mathbf{p}_m - \mathbf{p})/d_m$, and $d_m = \|\mathbf{p}_m - \mathbf{p}\|$.

B. Signal Model

The position of the mobile UE at measurement instance ℓ (i.e., ℓ -th pilot symbol) for $\ell \in \{1, \dots, L\}$ can be expressed $\mathbf{p}_\ell = \mathbf{p} + \mathbf{v}\ell T_s$ where $\mathbf{v}\ell T_s$ denotes the displacement induced by the velocity vector \mathbf{v} . Then, leveraging the model in [35], the received signal model at instance ℓ can be expressed in NF as¹

$$y_\ell = \alpha \mathbf{a}^\top(\mathbf{p}_\ell) \mathbf{\Omega}_\ell \mathbf{a}(\mathbf{p}_b) s_\ell + n_\ell \quad (1)$$

where \mathbf{p}_ℓ is a function of \mathbf{p} and \mathbf{v} , and s_ℓ denotes the transmitted pilot (taken as $s_\ell = 1, \forall \ell$ hereafter for ease of exposition), $\alpha \in \mathbb{C}$ is the complex channel gain that involves the impact of the transmit power, attenuation in both BS-RIS and RIS-UE paths and global phase offset, $\mathbf{\Omega}_\ell = \text{diag}(\boldsymbol{\omega}_\ell)$ with $\boldsymbol{\omega}_\ell \in \mathbb{C}^{M \times 1}$ denoting the vector of controlled RIS element-wise reflection coefficients, and $n_\ell \sim \mathcal{CN}(0, N_0)$ is an independent and identically distributed additive zero-mean normal noise of standard deviation N_0 . In (1), the element-wise RIS response model can be expressed as follows:

$$[\mathbf{a}(\mathbf{p}_\ell)]_m = \exp\left(-j \frac{2\pi}{\lambda} f_{\ell,m}(\mathbf{p}, \mathbf{v})\right), \quad (2)$$

$$f_{\ell,m}(\mathbf{p}, \mathbf{v}) = \|\mathbf{p}_m - (\mathbf{p} + \mathbf{v}\ell T_s)\| - \|\mathbf{p}_r - (\mathbf{p} + \mathbf{v}\ell T_s)\|, \quad (3)$$

$$\approx d_m - d_r + (\mathbf{u}_m(\mathbf{p}) - \mathbf{u}_r(\mathbf{p}))^\top \mathbf{v}\ell T_s, \quad (4)$$

where (4) is obtained from (3) after a Taylor series expansion and dropping higher-order terms (See Appendix A). It is worth noting that $\mathbf{a}(\mathbf{p}_b)$, which represents the RIS response vector corresponding to signals arriving from the BS, remains independent of ℓ since both the BS and the RIS are stationary entities. To have a compact model for the observations, we

¹We assume the absence of uncontrolled multipath in algorithm derivation [30], [36]. In the numerical results of Section IV, we will investigate the impact of uncontrolled multipath on estimation performance.

stack (1) over L symbols and define the observation vector $\mathbf{y} \triangleq [y_1 \dots y_L]^\top \in \mathbb{C}^{L \times 1}$, leading to

$$\mathbf{y} = \alpha \mathbf{h}(\mathbf{p}, \mathbf{v}) + \mathbf{n}, \quad (5)$$

$$\mathbf{h}(\mathbf{p}, \mathbf{v}) \triangleq [h_1(\mathbf{p}, \mathbf{v}) \dots h_L(\mathbf{p}, \mathbf{v})]^\top \in \mathbb{C}^{L \times 1}, \quad (6)$$

$$h_\ell(\mathbf{p}, \mathbf{v}) \triangleq \mathbf{w}_\ell^\top \mathbf{a}(\mathbf{p}_\ell), \quad (7)$$

where $\mathbf{n} \triangleq [n_1 \dots n_L]^\top$ and $\mathbf{w}_\ell \triangleq \boldsymbol{\omega}_\ell \odot \mathbf{a}(\mathbf{p}_b) \in \mathbb{C}^{M \times 1}$.

C. Problem Description and Maximum-Likelihood Estimator

Given the NLoS RIS-induced observations (5) at the mobile UE, our goal is to perform joint estimation of its position \mathbf{p} and velocity \mathbf{v} , along with the nuisance parameter α . For this problem, the maximum likelihood (ML) estimator of the unknown parameter vector $\boldsymbol{\zeta} = [\mathbf{p}^\top, \mathbf{v}^\top, \alpha]^\top$ can be expressed as

$$(\hat{\alpha}, \hat{\mathbf{p}}, \hat{\mathbf{v}}) = \arg \min_{\alpha, \mathbf{p}, \mathbf{v}} \|\mathbf{y} - \alpha \mathbf{h}(\mathbf{p}, \mathbf{v})\|^2, \quad (8)$$

which involves a high-dimensional search. Alternatively, the ML estimator of \mathbf{p} and \mathbf{v} can be obtained by the closed-form (CF) estimation of α in (8):

$$\hat{\alpha} = \frac{\mathbf{h}^\text{H}(\mathbf{p}, \mathbf{v}) \mathbf{y}}{\|\mathbf{h}(\mathbf{p}, \mathbf{v})\|^2}. \quad (9)$$

Plugging (9) back into (8), we obtain the concentrated cost function

$$(\hat{\mathbf{p}}, \hat{\mathbf{v}}) = \arg \min_{\mathbf{p}, \mathbf{v}} \left\| \mathbf{\Pi}_{\mathbf{h}(\mathbf{p}, \mathbf{v})}^\perp \mathbf{y} \right\|^2, \quad (10)$$

leading to a 6D optimization problem. In the subsequent sections, our focus will be directed towards solving (8), and when convenient, its concentrated form (10), with an emphasis on achieving low computational complexity.

III. PROPOSED METHOD

In this section, we will elaborate on the overall procedure of estimating the 6D position and velocity parameters of the mobile UE in the absence of prior knowledge.

A. Top-Down Description

The overall method is described in Algorithm 1. The methods commence by assuming a static UE with unknown position, and then iterates between velocity and position estimations until the objective function (8) converges. A final, Quasi-Newton, refinement routine is performed to better estimate the positional, velocity, and gain parameters. The subroutines `InitPosGain`(\mathbf{y}) and `RefVel`($\mathbf{y}, \hat{\mathbf{v}}, \hat{\mathbf{p}}, \hat{\alpha}$) will be described in Section III-B, and the subroutine `RefPosGain`($\mathbf{y}, \hat{\mathbf{v}}, \hat{\mathbf{p}}, \hat{\alpha}$) will be detailed in Section III-C.

Algorithm 1 6D Estimation in RIS-Aided Near-Field Localization: $(\widehat{\alpha}, \widehat{\mathbf{p}}, \widehat{\mathbf{v}}) = \text{FindPosVel}(\mathbf{y})$

- 1: **Input:** Observation \mathbf{y} in (5).
- 2: **Output:** Position, velocity and gain estimates $\widehat{\alpha}, \widehat{\mathbf{p}}, \widehat{\mathbf{v}}$.
- 3: Initialize the velocity estimate as $\widehat{\mathbf{v}} = \mathbf{0}$ m/s.
- 4: Initialize the position and gain estimates

$$(\widehat{\mathbf{p}}, \widehat{\alpha}) = \text{InitPosGain}(\mathbf{y}) .$$

- 5: **While** the objective in (8) does not converge
- 6: Update the velocity and gain estimates

$$(\widehat{\mathbf{v}}, \widehat{\alpha}) \leftarrow \text{RefVel}(\mathbf{y}, \widehat{\mathbf{v}}, \widehat{\mathbf{p}}, \widehat{\alpha}) .$$

- 7: Update the position and gain estimates

$$(\widehat{\mathbf{p}}, \widehat{\alpha}) \leftarrow \text{RefPosGain}(\mathbf{y}, \widehat{\mathbf{v}}, \widehat{\mathbf{p}}, \widehat{\alpha}) .$$

- 8: **end while**

- 9: Perform 6D gradient descent search, starting from $(\widehat{\mathbf{p}}, \widehat{\mathbf{v}})$.
 - 10: Update $\widehat{\alpha}$ via (9).
-

B. Position Estimate with Known Velocity

The proposed estimation algorithm is an extension to that proposed in [35]. Injecting the estimate of α from (9) back into (8), the ML estimate of \mathbf{p} can be computed as

$$\widehat{\mathbf{p}} = \arg \min_{\mathbf{p}} \left\| \mathbf{\Pi}_{\mathbf{h}(\mathbf{p}, \mathbf{v})}^{\perp} \mathbf{y} \right\|^2 . \quad (11)$$

Since solving (11) still requires a 3D search, we propose the first subroutine, which provides an initial coarse position estimate with reduced complexity (2D search and 1D search), followed by an extremely efficient refinement with linear approximation.

1) *Coarse Estimate:* We first assume that the UE is static (i.e., $\mathbf{v} = \mathbf{0}$ m/s), then the velocity effects in the RIS response model of (2), as well as the dependency on the time index ℓ disappear. Hence, the simplified response model becomes

$$[\mathbf{a}(\mathbf{p})]_m = \exp \left(-j \frac{2\pi}{\lambda} (d_m - d_r) \right) . \quad (12)$$

Accordingly, we define $\mathbf{W} \triangleq [\mathbf{w}_1 \dots \mathbf{w}_L] \in \mathbb{C}^{M \times L}$ and $\mathbf{h}(\mathbf{p}, \mathbf{0}) \triangleq \mathbf{W}^{\top} \mathbf{a}(\mathbf{p})$, then the ML estimator in (11) can now be expressed as

$$\widehat{\mathbf{p}} = \arg \min_{\mathbf{p}} \left\| \mathbf{\Pi}_{\mathbf{W}^{\top} \mathbf{a}(\mathbf{p})}^{\perp} \mathbf{y} \right\|^2 . \quad (13)$$

To solve (13), we utilize a first-order Taylor expansion to approximate the generic NF RIS response in (12) by its FF version as [See Appendix B]

$$[\mathbf{a}(\mathbf{p})]_m \approx [\mathbf{a}(\phi, \theta)]_m = \exp(-j(\mathbf{p}_m - \mathbf{p}_r)^{\top} \mathbf{k}(\phi, \theta)) , \quad (14)$$

where $\mathbf{k}(\phi, \theta) = -\frac{2\pi}{\lambda} [\sin \phi \cos \theta, \sin \phi \sin \theta, \cos \phi]^{\top}$. Leveraging the approximated model in (14), we performed a 2D search over $\theta \in [0, 2\pi]$ in azimuth and $\phi \in [0, \pi/2]$ in elevation to find $\widehat{\theta}$ and $\widehat{\phi}$, respectively:

$$(\widehat{\theta}, \widehat{\phi}) = \arg \min_{\theta, \phi} \left\| \mathbf{\Pi}_{\mathbf{W}^{\top} \mathbf{a}(\theta, \phi)}^{\perp} \mathbf{y} \right\|^2 . \quad (15)$$

Algorithm 2 Initialize Position and Gain Estimate: $(\widehat{\mathbf{p}}, \widehat{\alpha}) = \text{InitPosGain}(\mathbf{y})$

- 1: **Input:** Observation \mathbf{y} in (5).
 - 2: **Output:** Initial position estimate $\widehat{\mathbf{p}}$, initial gain estimate $\widehat{\alpha}$.
 - 3: Find initial θ and ϕ estimates by solving (15).
 - 4: **While** (16) and (17) do not converge
 - 5: Update the distance estimate via (16).
 - 6: Update the azimuth and elevation estimate via (17).
 - 7: **end while**
 - 8: Compute the initial position estimate $\widehat{\mathbf{p}}$.
 - 9: Compute the initial gain estimate $\widehat{\alpha}$ via (9).
-

Then, based on the estimated angles, a linear distance search is performed

$$\widehat{\rho} = \arg \min_{\rho} \left\| \mathbf{\Pi}_{\mathbf{W}^{\top} \mathbf{a}(\rho, \widehat{\theta}, \widehat{\phi})}^{\perp} \mathbf{y} \right\|^2 , \quad (16)$$

to find $\widehat{\rho}$, using the NF model (12). The steps (15)–(16) were proposed in [35]. We extend the method by iteratively refining the 2D angle estimate with the NF model

$$(\widehat{\theta}, \widehat{\phi}) = \arg \min_{\theta, \phi} \left\| \mathbf{\Pi}_{\mathbf{W}^{\top} \mathbf{a}(\rho, \theta, \phi)}^{\perp} \mathbf{y} \right\|^2 , \quad (17)$$

and the distance estimate using (16). The entire procedure is summarized in Algorithm 2.

2) *Refinement via Linearization:* We now present the second subroutine, which is a local refinement to refine the coarse position estimate \mathbf{p}_0 and account for the fact that the velocity is in reality non-zero. For that, we propose to linearize the phase term in the initial steering vector (2) around \mathbf{p}_0 to obtain a first-order approximation, then a small angle approximation (SAA) is performed and the new ML estimator is hence derived. The linearized RIS response model can now be expressed as

$$[\mathbf{a}(\mathbf{p}_\ell)]_m \approx [\widetilde{\mathbf{a}}(\mathbf{p}_0)]_m \triangleq \exp \left(-j \frac{2\pi}{\lambda} \left\{ f_{\ell, m}(\mathbf{p}_0, \mathbf{v}) + (\mathbf{p} - \mathbf{p}_0)^{\top} \nabla_{\mathbf{p}} f_{\ell, m}(\mathbf{p}, \mathbf{v})|_{\mathbf{p}=\mathbf{p}_0} \right\} \right) , \quad (18)$$

where $\widetilde{\mathbf{a}}(\mathbf{p}_0)$ is the linearization of $\mathbf{a}(\mathbf{p}_\ell)$ around \mathbf{p}_0 , $f_{\ell, m}(\mathbf{p}, \mathbf{v})$ is defined in (4) and its gradient $\nabla_{\mathbf{p}} f_{\ell, m}(\mathbf{p}, \mathbf{v})$ is derived in Appendix C. Since the right-hand side of (18) depends on \mathbf{p} only via $\mathbf{p}_\delta \triangleq \mathbf{p} - \mathbf{p}_0$, we can change the unknown from \mathbf{p} to \mathbf{p}_δ , which results in

$$[\widetilde{\mathbf{a}}(\mathbf{p}_0 + \mathbf{p}_\delta)]_m = \exp \left(j [b_{\ell, m} + \mathbf{p}_\delta^{\top} \mathbf{c}_{\ell, m}] \right) , \quad (19)$$

$$b_{\ell, m} \triangleq -\frac{2\pi}{\lambda} f_{\ell, m}(\mathbf{p}_0, \mathbf{v}) , \quad (20)$$

$$\mathbf{c}_{\ell, m} \triangleq -\frac{2\pi}{\lambda} \nabla_{\mathbf{p}} f_{\ell, m}(\mathbf{p}, \mathbf{v})|_{\mathbf{p}=\mathbf{p}_0} \in \mathbb{R}^{3 \times 1} . \quad (21)$$

Here, the dependence of $b_{\ell, m}$ and $\mathbf{c}_{\ell, m}$ on \mathbf{v} is dropped for the sake of notation convenience (and because \mathbf{v} is known). Since \mathbf{p}_δ is expected to be small, we can invoke SAA in (19) to obtain

$$[\widetilde{\mathbf{a}}(\mathbf{p}_0 + \mathbf{p}_\delta)]_m \approx \exp(j b_{\ell, m}) (1 + j \mathbf{p}_\delta^{\top} \mathbf{c}_{\ell, m}) , \quad (22)$$

Algorithm 3 Refine Position and Gain Estimate with Fixed Velocity: $(\widehat{\mathbf{p}}, \widehat{\alpha}) = \text{RefPosGain}(\mathbf{y}, \mathbf{v}, \mathbf{p}_0, \alpha_0)$

- 1: **Input:** Observation \mathbf{y} in (5), velocity \mathbf{v} , initial position estimate \mathbf{p}_0 , and initial gain estimate α_0 .
 - 2: **Output:** Refined position estimate $\widehat{\mathbf{p}}$, refined gain estimate $\widehat{\alpha}$.
 - 3: Set $\widehat{\alpha} = \alpha_0$.
 - 4: **while** the objective in (27) does not converge
 - 5: Compute $\boldsymbol{\eta}$ and $\boldsymbol{\Xi}$ in (27) using \mathbf{v} and \mathbf{p}_0 .
 - 6: Update the residual position estimate $\widehat{\mathbf{p}}_\delta$ via (28).
 - 7: Update the gain estimate $\widehat{\alpha}$ via (29).
 - 8: **end while**
 - 9: Refine the position estimate by setting $\widehat{\mathbf{p}} = \mathbf{p}_0 + \widehat{\mathbf{p}}_\delta$.
-

Based on the approximation in (22), we can compute $h_\ell(\mathbf{p}, \mathbf{v})$ in (7) as

$$h_\ell(\mathbf{p}_0 + \mathbf{p}_\delta, \mathbf{v}) = \mathbf{w}_\ell^\top \widetilde{\boldsymbol{\alpha}}(\mathbf{p}_0 + \mathbf{p}_\delta) \quad (23)$$

$$= \sum_{m=1}^M [\mathbf{w}_\ell]_m [\widetilde{\boldsymbol{\alpha}}(\mathbf{p}_0 + \mathbf{p}_\delta)]_m \quad (24)$$

$$\approx \boldsymbol{\eta}_\ell + j\mathbf{p}_\delta^\top \boldsymbol{\xi}_\ell, \quad (25)$$

where $\boldsymbol{\eta}_\ell \triangleq \sum_{m=1}^M [\mathbf{w}_\ell]_m \exp(jb_{\ell,m})$ and $\boldsymbol{\xi}_\ell \triangleq \sum_{m=1}^M [\mathbf{w}_\ell]_m \exp(jb_{\ell,m}) \mathbf{c}_{\ell,m}$. Introducing $\boldsymbol{\eta} \triangleq [\eta_1 \dots \eta_L]^\top \in \mathbb{C}^{L \times 1}$ and $\boldsymbol{\Xi} \triangleq [\boldsymbol{\xi}_1 \dots \boldsymbol{\xi}_L] \in \mathbb{C}^{3 \times L}$, $\mathbf{h}(\mathbf{p} = \mathbf{p}_0 + \mathbf{p}_\delta, \mathbf{v})$ in (6) becomes

$$\mathbf{h}(\mathbf{p}_0 + \mathbf{p}_\delta, \mathbf{v}) \approx \boldsymbol{\eta} + j\boldsymbol{\Xi}^\top \mathbf{p}_\delta, \quad (26)$$

which implies that the ML estimator (8) can be approximated as

$$(\widehat{\alpha}, \widehat{\mathbf{p}}_\delta) = \arg \min_{\alpha, \mathbf{p}_\delta} \|\mathbf{y} - \alpha(\boldsymbol{\eta} + j\boldsymbol{\Xi}^\top \mathbf{p}_\delta)\|^2, \quad (27)$$

where we recall that we estimate the residual position \mathbf{p}_δ instead of the actual position \mathbf{p} . We propose to solve (27) via alternating updates of α and \mathbf{p}_δ , yielding (see Appendix D)

$$\widehat{\mathbf{p}}_\delta = \frac{1}{|\widehat{\alpha}|^2} (\text{Re}\{\boldsymbol{\Xi}^* \boldsymbol{\Xi}^\top\})^{-1} \text{Im}\{\boldsymbol{\Xi}(|\widehat{\alpha}|^2 \boldsymbol{\eta}^* - \widehat{\alpha} \mathbf{y}^*)\}, \quad (28)$$

$$\widehat{\alpha} = \frac{(\boldsymbol{\eta} + j\boldsymbol{\Xi}^\top \widehat{\mathbf{p}}_\delta)^\text{H} \mathbf{y}}{\|\boldsymbol{\eta} + j\boldsymbol{\Xi}^\top \widehat{\mathbf{p}}_\delta\|^2}. \quad (29)$$

Algorithm 3 summarizes the above procedure.

C. Velocity Estimate with Known Position

In this section, we present an iterative refinement routine, in closed form, to estimate the velocity of the UE assuming knowledge over its position. The procedure is similar to Section III-B but operating on residual velocity rather than residual position. Since the velocity already appears linearly in the argument of the exponential in the steering vector, the first linearization step is not needed for this algorithm.

We denote by \mathbf{v}_0 the initial velocity estimate and $\mathbf{v}_\delta = \mathbf{v} - \mathbf{v}_0$ the velocity residual resulting from estimation inaccuracies. The RIS response (2) can be expressed as

$$[\mathbf{a}(\mathbf{p}_\ell)]_m = e^{j\beta_m} \exp(j\mathbf{v}^\top \boldsymbol{\gamma}_m \ell T_s), \quad (30)$$

Algorithm 4 Refine Velocity Estimate with Fixed Position and Gain: $\widehat{\mathbf{v}} = \text{RefVel}(\mathbf{y}, \mathbf{v}_0, \mathbf{p}, \alpha)$

- 1: **Input:** Observation \mathbf{y} in (5), position \mathbf{p} , initial velocity estimate \mathbf{v}_0 , and gain α_0 .
 - 2: **Output:** Refined velocity estimate $\widehat{\mathbf{v}}$, refined gain estimate $\widehat{\alpha}$.
 - 3: Set $\widehat{\alpha} = \alpha_0$.
 - 4: **while** the objective in (34) does not converge
 - 5: Compute $\boldsymbol{\nu}$ and \mathbf{M} in (34) using \mathbf{p} and \mathbf{v}_0 .
 - 6: Update the residual velocity estimate $\widehat{\mathbf{v}}_\delta$ via (35).
 - 7: Update the gain estimate $\widehat{\alpha}$ via (36).
 - 8: **end while**
 - 9: Refine the velocity estimate by setting $\widehat{\mathbf{v}} = \mathbf{v}_0 + \widehat{\mathbf{v}}_\delta$.
-

where $\beta_m = -\frac{2\pi}{\lambda} (\|\mathbf{p}_m - \mathbf{p}\| - \|\mathbf{p}_r - \mathbf{p}\|)$ and $\boldsymbol{\gamma}_m = -\frac{2\pi}{\lambda} (\mathbf{u}_m(\mathbf{p}) - \mathbf{u}_r(\mathbf{p}))$. Note that the dependence of β_m and $\boldsymbol{\gamma}_m$ on \mathbf{p} is dropped for notational convenience because \mathbf{p} is given. We then express the latter in terms of the residual velocity \mathbf{v}_δ as

$$[\mathbf{a}(\mathbf{p}_\ell)]_m = e^{j\beta_m} \exp(j\mathbf{v}_0^\top \boldsymbol{\gamma}_m \ell T_s) \exp(j\mathbf{v}_\delta^\top \boldsymbol{\gamma}_m \ell T_s), \quad (31)$$

and linearize around \mathbf{v}_δ , which we expect to be small, by employing the SAA

$$[\mathbf{a}(\mathbf{p}_\ell)]_m \approx e^{j\beta_m} \exp(j\mathbf{v}_0^\top \boldsymbol{\gamma}_m \ell T_s) (1 + j\mathbf{v}_\delta^\top \boldsymbol{\gamma}_m \ell T_s). \quad (32)$$

Based on this approximation we then compute the terms in (7) reflecting (32) as $[h_\ell(\mathbf{p}, \mathbf{v}_0 + \mathbf{v}_\delta)]_m = \sum_{m=1}^M [\mathbf{w}_\ell]_m [\mathbf{a}(\mathbf{p}_\ell)]_m \approx \nu_\ell + \mathbf{v}_\delta^\top \boldsymbol{\mu}_\ell$ where $\nu_\ell = \sum_{m=1}^M [\mathbf{w}_\ell]_m \exp(j\beta_m) \exp(j\mathbf{v}_0^\top \boldsymbol{\gamma}_m \ell T_s)$, and $\boldsymbol{\mu}_\ell = \sum_{m=1}^M j[\mathbf{w}_\ell]_m \exp(j\beta_m) \exp(j\mathbf{v}_0^\top \boldsymbol{\gamma}_m \ell T_s) \boldsymbol{\gamma}_m \ell T_s$. Using the definition in (6), the vector form of $h_\ell(\mathbf{p}, \mathbf{v}_0 + \mathbf{v}_\delta)$ can be expressed as

$$\mathbf{h}(\mathbf{p}, \mathbf{v}_0 + \mathbf{v}_\delta) \approx \boldsymbol{\nu} + \mathbf{M}^\top \mathbf{v}_\delta, \quad (33)$$

where $\boldsymbol{\nu} \triangleq [\nu_1 \dots \nu_L]^\top$ and $\mathbf{M} \triangleq [\boldsymbol{\mu}_1 \dots \boldsymbol{\mu}_L]^\top \in \mathbb{C}^{3 \times L}$. The ML estimation for the residual velocity from (8) can be expressed as

$$(\widehat{\alpha}, \widehat{\mathbf{v}}_\delta) = \arg \min_{\alpha, \mathbf{v}_\delta} \|\mathbf{y} - \alpha(\boldsymbol{\nu} + j\mathbf{M}^\top \mathbf{v}_\delta)\|^2, \quad (34)$$

We propose to solve (34) via alternating updates of α and \mathbf{v}_δ , yielding

$$\widehat{\mathbf{v}}_\delta = \frac{1}{|\widehat{\alpha}|^2} (\text{Re}\{\mathbf{M}^* \mathbf{M}^\top\})^{-1} \text{Im}\{\mathbf{M}(|\widehat{\alpha}|^2 \boldsymbol{\nu}^* - \widehat{\alpha} \mathbf{y}^*)\}, \quad (35)$$

$$\widehat{\alpha} = \frac{(\boldsymbol{\nu} + j\mathbf{M}^\top \widehat{\mathbf{v}}_\delta)^\text{H} \mathbf{y}}{\|\boldsymbol{\nu} + j\mathbf{M}^\top \widehat{\mathbf{v}}_\delta\|^2}. \quad (36)$$

Note that here as well, the mild condition of $L \geq 3$ transmissions is required to compute the closed form UE velocity using (35). Algorithm 4 summarizes the procedure.

D. Time Complexity Analysis

We now present the complexity scaling of the algorithms as a function of the RIS size M and number of pilot transmissions L , as well as the number of iterations in Algorithm 1, Algorithm 2, Algorithm 3, and Algorithm 4, denoted by $I_1, I_2, I_3,$

and I_4 , respectively. We denote the complexity of Algorithm i by \mathcal{C}_i .

We find that $\mathcal{C}_3 = \mathcal{O}(I_3LM)$ and $\mathcal{C}_4 = \mathcal{O}(I_4LM)$, mainly due to the computation of line 5 (i.e., $\boldsymbol{\eta}$, $\boldsymbol{\Xi}$, $\boldsymbol{\nu}$, and \boldsymbol{M}) in both methods. Moving this line before the while loop will turn out to not severely affect performance, but leads to a significant complexity reduction $\mathcal{C}_3 = \mathcal{O}(I_3L)$ and $\mathcal{C}_4 = \mathcal{O}(I_4L)$. It is also readily verified that $\mathcal{C}_2 = \mathcal{O}(LMI_2 \max\{K_\theta \times K_\phi, K_\rho\})$, where K_θ (resp. K_ϕ and K_ρ) denotes the grid size for the search over θ (resp. ϕ , ρ).

Finally, introducing I_{GD} as the number of gradient descent iterations, we find that

$$\mathcal{C}_1 = \mathcal{C}_2 + I_1(\mathcal{C}_3 + \mathcal{C}_4) + \mathcal{O}(I_{\text{GD}}LM) \quad (37)$$

$$= \mathcal{O}(LMI_2 \max\{K_\theta \times K_\phi, K_\rho\}) + \mathcal{O}(I_1I_3L) \\ + \mathcal{O}(I_1I_4L) + \mathcal{O}(I_{\text{GD}}LM), \quad (38)$$

provided line 5 is moved before the while loop in Algorithms 3–4.

IV. NUMERICAL SIMULATIONS AND RESULTS

In order to evaluate the effectiveness of the proposed estimation framework, numerical simulations were conducted in a canonical indoor scenario.

A. Scenario Definition and Performance Metrics

In the following, we consider random RIS phase profile design and we list, in Table I, the scenario parameters [28]. We evaluate the performance of the algorithmic variants introduced in section III (under different prior knowledge assumptions), while comparing them with both theoretical bounds and that of a state-of-the-art (SoTA) algorithm assuming zero velocity from [35]. In the following, we refer to the algorithms as follows:

- *Grid search (GS)*: This method refers to Algorithm 2, providing a position estimate assuming a zero velocity.
- *CF Position Refinement*: This method refers to the closed-form position refinement routine of Algorithm 3.
- *CF Velocity Refinement*: This method refers to the closed-form velocity refinement procedure of Algorithm 4.
- *Global Refinement*: This method is the 6D gradient descent in Algorithm 1, line 9, which is used to enhance the accuracy of both position and velocity estimation.

We also assess the sensitivity of the proposed approach to critical system parameters, such as the distance to the RIS, the norm of the velocity vector, or small-scale fading effects resulting from uncontrolled multipath components (i.e., besides the used RIS-reflected path). In terms of geometry, the RIS is located at the xy -plane center and the UE's position is defined as $\boldsymbol{p} = \rho \boldsymbol{i}$ where $\rho \in [1, 10]$ m denotes the RIS-UE distance and $\boldsymbol{i} = [-1, 2, 1]^T / \|[-1, 2, 1]^T\|$ acts as a unit vector. Similarly, the UE's velocity is defined as $\boldsymbol{v} = v \boldsymbol{i}$ where $v \in [0, 20]$ m/s denotes the speed.² According to the approximation in Appendix A, the UE speed v should be below the limit computed via (43), given

²Note that the velocity vector utilized in the simulations is radial w.r.t. the RIS. We have verified that the proposed algorithms operate close to the corresponding bounds, for other velocity vectors as well.

parameter	value	parameter	value
Frequency	$f_c = 28$ GHz	Wavelength	$\lambda_c \approx 1.07$ cm
Bandwidth	$W = 1$ MHz	Power transmitted	$P_{\text{Tx}} = 20$ dBm
Noise PSD	$N_0 = -174$ dBm/Hz	Noise figure	$n_f = 8$ dB
RIS loc.	$\boldsymbol{p}_r = [0, 0, 0]^T$ m	BS loc.	$\boldsymbol{p}_b = [3, 3, 1]^T$ m
RIS size	$M = 32 \times 32$ elements	Transmissions	$L = 40$

TABLE I: General simulation parameters.

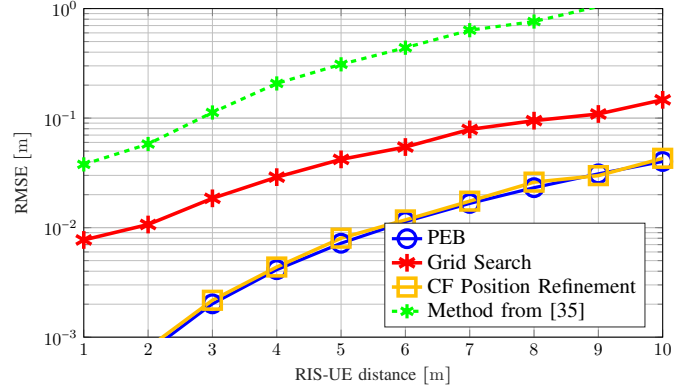


Fig. 2: RMSE of position estimation with known UE velocity ($v = 1$ m/s) using Algorithms 2 and 3, along with the corresponding PEB, as a function of the RIS-UE distance.

the parameters in Table I. More precisely, a minimum distance condition $\|\boldsymbol{\delta}_m\| > 1$ m, $\forall m$ is considered, as well as maximum values for $L = 50$ and $T_s = 100 \mu\text{s}$. Under these settings, the condition $\|\boldsymbol{v}\| LT_s \ll \|\boldsymbol{\delta}_m\|$, $\forall m$ simplifies to $\|\boldsymbol{v}\| \ll 200$ m/s, a condition that aligns with our simulations as we consider speeds up to 20 m/s.

Performance is evaluated through the root mean squared error (RMSE) of the position and velocity, which is calculated over 1000 random measurement noise realizations for each tested UE position-velocity configuration. The RMSEs are compared to the corresponding error bounds, PEB and VEB.

We found that in Algorithms 3 and 4, when the linearization in line 5 is only executed once before the loop instead of every iteration, the performance is nearly identical to performing the linearization every iteration. Given the complexity analysis in Section III-D, from now on we only use this low-complexity version the CF refinement methods.

B. Performance of 3D Estimation

We first discuss the performance of the 3D estimation algorithms for position and velocity separately.

1) *Position Estimation with Known Velocity*: First, in Fig. 2, we show the RMSE of the position estimation for the two algorithmic steps of Section III-B, along with the corresponding PEB, as a function of the RIS-UE distance and with a fixed velocity of $v = 1$ m/s. One can notice that the PEB (in blue) remains at a sub-cm level at short RIS-UE distances (i.e., below 6 m) but then increases up to a few cm as the UE moves away from the RIS. The first part of our estimation routine, which relies on GS (in red) routine in 2, apparently suffers from a big performance gap compared to the bound, this is caused by the multiple approximations made during the development of this algorithm (See Section III-B). However, feeding the output of this initial search routine into the CF position refinement routine (in amber), i.e., Algorithm 3 enables to reach the

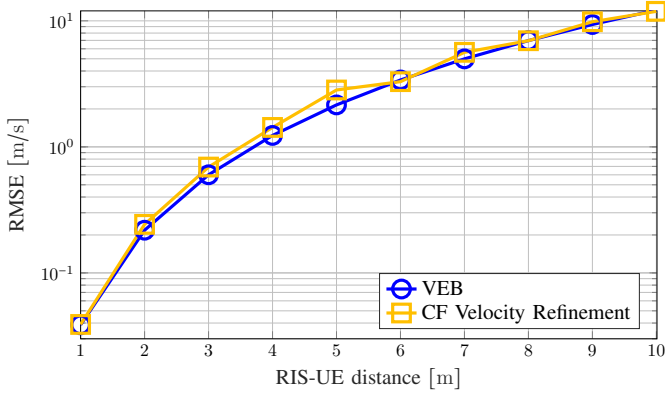


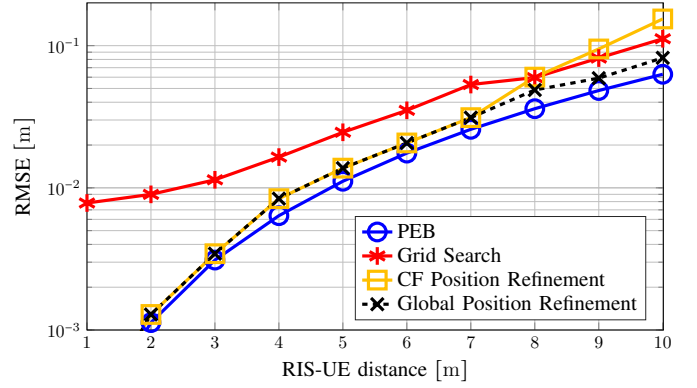
Fig. 3: RMSE of velocity estimation with known position and an unknown velocity ($v = 1$ m/s) (i.e., Algorithm 4) and corresponding VEB as a function of RIS-UE distance.

performance bound, whatever the distance. To better assess the performance of our algorithm, we have also benchmarked our algorithm with the closest contribution from the SoTA. More specifically, in [35], the authors devised a grid-search-based algorithm to estimate the position of the UE by exploiting the signal's wavefront curvature. This approach accounts for the effects of geometric NF on positioning while assuming no velocity in the model. The method from [35] involves three distinct 1D search procedures over the three spherical dimensions. For this purpose, they performed a Jacobi Anger expansion to be able to separate both angles in the RIS model. Fig. 2 shows that the method from [35] leads to a significant performance degradation.

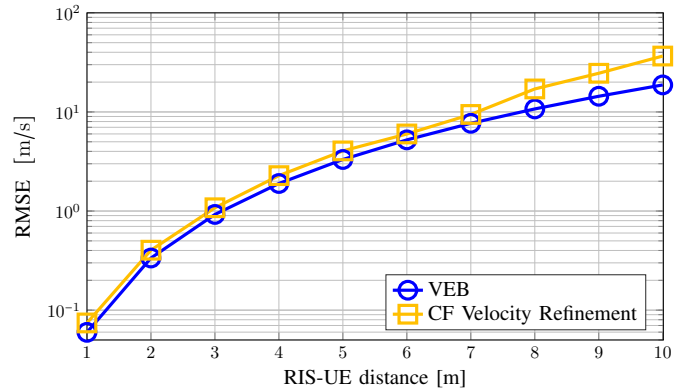
2) *Velocity Estimation with Known Position*: In Fig. 3, we show the RMSE of velocity estimation for the refinement algorithm of Section III-C, along with the corresponding VEB, still as a function of the RIS-UE distance. Without loss of generality, the actual velocity value was set to 1 m/s in this example, but further studies include higher values to evaluate the sensitivity to more extreme UE mobility (see Section IV-D1). Note that the tested algorithm does not include an extensive grid search like before, but uniquely the CF velocity refinement routine, which is called with an initial velocity value of 0 m/s. We thus observe that the RMSE of this estimation almost coincides with the VEB curve, regardless of the RIS-UE distance.

C. Performance of 6D estimation

After simulating the 3D position and 3D velocity estimation algorithms separately, we now evaluate the performance of 6D position and velocity estimation with no prior knowledge regarding the UE state. Figs. 4a and 4b first show the RMSE of position and velocity estimation respectively, alongside their related theoretical bounds, versus the RIS-UE distance for a static UE, i.e., with $v = 1$ m/s. The curves in Fig. 4a show that Algorithm 2 (GS - in red) alone does not perform well compared to the PEB, especially at short distance, whereas Algorithm 3 (CF Refinement routine - in amber) significantly boosts the estimation performance at short distances, and even touches the PEB curve at short-to-mid ranges. However, as the



(a) RMSE of position estimation and related PEB versus RIS-UE distance.



(b) RMSE of velocity estimation and related VEB versus RIS-UE distance.

Fig. 4: 6D estimation errors and related theoretical bounds versus RIS-UE distance, for a constant UE velocity ($v = 1$ m/s).

RIS-UE distance increases, we notice a drop in performance, this is caused by implementing the approximation in (22) whose error increases as the UE moves further from the RIS. For this reason, a Global Refinement (in dashed black) routine has been implemented to enhance estimation mostly at far distances, where the previous algorithms fail.

D. Sensitivity Analyses

Now that we have established the performance of the proposed method and its ability to attain the CRLBs, we move on to study the sensitivity to the speed, to uncontrolled multipath, and to the SNR.

1) *Sensitivity to the Speed*: The same simulation setup is now used to study the effect of the UE's velocity on our algorithms. Thus, we assume a dynamic UE, with a velocity varying from 0 m/s to around 50 m/s, while the RIS-UE distance is set to 2 m. The corresponding results are displayed in Fig. 5. We can hence see clearly the negative effect of large velocity on the GS algorithm, while the rest of the other routines still continue performing well, in compliance with the PEB behavior, suggesting that our overall estimation framework is fairly robust against high UE mobility.

2) *Sensitivity to Uncontrolled Multipath*: We now discuss the performance in the presence of a multipath-rich channel. The BS is considered to be directive, and hence only one LoS path exists in the BS-RIS channel [37], [38]. On the other

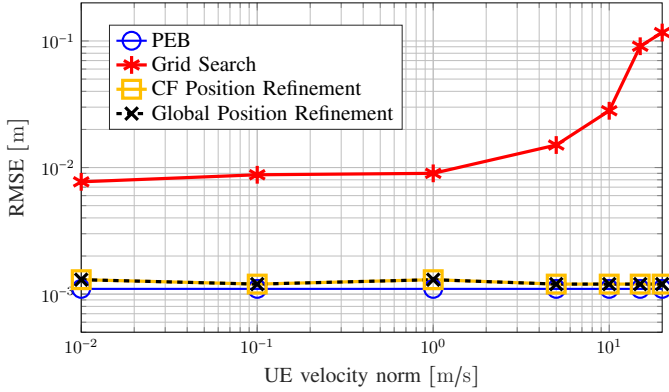


Fig. 5: UE's mobility effect on the position estimation and PEB in NF. The RIS-UE distance is set to $\rho = 2$ m.

hand, the channel between the RIS and the UE is modeled as Rician [39], [40], which yields a change in the signal model of (1) into

$$y_\ell = \alpha \left(\sqrt{\frac{\mathcal{K}}{\mathcal{K}+1}} \mathbf{a}(\mathbf{p}_\ell) + \sqrt{\frac{1}{\mathcal{K}+1}} \tilde{\mathbf{h}} \right)^\top \Omega_\ell \mathbf{a}(\mathbf{p}_b) + n_\ell, \quad (39)$$

where $\tilde{\mathbf{h}} \in \mathbb{C}^{M \times 1}$ is the NLoS³ component of the RIS-UE channel with $\tilde{\mathbf{h}} \sim \mathcal{CN}(\mathbf{0}, \mathbf{I})$ and \mathcal{K} is the Rician factor. From (39), we notice that $\mathcal{K} \rightarrow 0$ results in a Rayleigh channel which translates to losing the LoS path between the RIS and UE. Fig. 6 depicts the effect of the multipath profile introduction on the proposed position estimation algorithms, more precisely, Algorithms 2 and 3 as a function of $\mathcal{K} \in [5, 10^3]$, while the RIS-UE distance is set to 2 m. We also plot the PEB of the same scenario (in terms of velocity and distance) but without any multipath for the sake of benchmarking. We notice that, as \mathcal{K} increases, the RMSE levels of both algorithms improve but coincide until around $\mathcal{K} \approx 10^2$ where the refinement routine surpasses the GS output and starts operating normally again. Finally, as $\mathcal{K} \approx 10^3$, a significant drop in the RMSE of the refinement algorithm is noticed while that of the GS seems to decrease more slowly, but both algorithms follow the trend approaching the PEB values. Mitigating a bit the results of the previous sensitivity analysis, and in light of comments from [41] regarding the validity of small-scale fading models in the mmWave domain, we recall that the combined effects of spatial filtering (thanks to large antenna arrays) and higher power path losses would anyway lead to the reception of relatively sparse and weak secondary multipath components (besides the direct RIS-UE path) in our case.

3) *Sensitivity to SNR*: We also evaluated the performance of our system w.r.t. SNR. Thus, in Fig. 7 we have plotted the PEB performance alongside our devised estimation routines as we change the SNR, all while fixing the RIS-UE distance and UE velocity to 5 m and 1 m/s respectively. We first notice that the PEB follows an expected trend of linearly decreasing with higher SNR values. On the other hand, Algorithm 2 does not achieve acceptable levels of accuracy at very low SNR values,

³The NLoS is herein defined with respect to the direct path from the RIS to the UE and accounts for the effect of the uncontrolled multipath components besides this direct path.

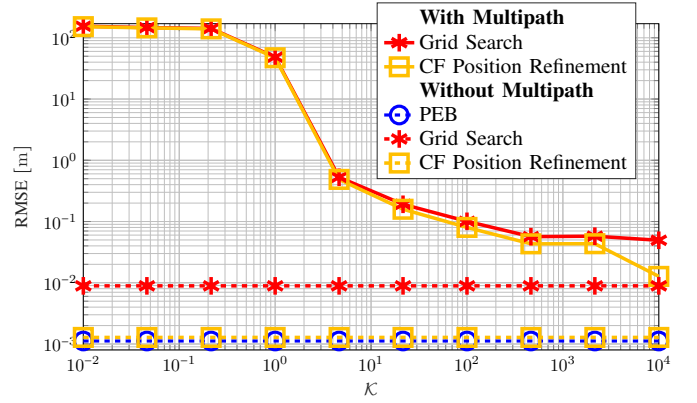


Fig. 6: RMSE of position estimation for the proposed GS and CF refinement algorithms versus the multipath Rician \mathcal{K} -factor. The RIS-UE distance is set to $\rho = 2$ m and the UE's velocity to $v = 1$ m/s, and $\mathcal{K} \in [5, 10^3]$.

which means that no localization service could be guaranteed at such conditions. However, as the SNR hits -20 dB, the performance of the aforementioned algorithm is boosted to the point where it touches the PEB, and then continuous at that same level even if the SNR is significantly increased. This saturation is due to the finite grid resolution used in this algorithm. Finally, it is noticeable that the CF position refinement algorithm fail completely at very low SNR, but then, also at -20 dB its performance comes back and it follows the trend of the PEB; and of course, since its output is fed as input to the global refinement algorithm, the latter follows the same trend as well.

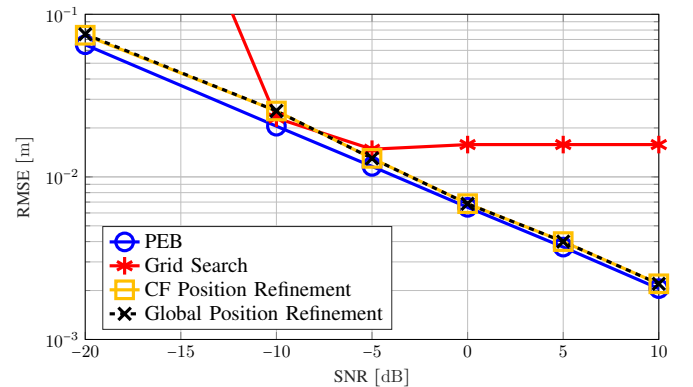


Fig. 7: RMSE of position estimation for the proposed Algorithms 2 and 3 versus the SNR. The RIS-UE distance is set to $\rho = 5$ m and the UE's velocity to $v = 1$ m/s, as a function of the SNR.

E. Convergence

Finally, we empirically illustrate the average convergence rates (over all the Monte Carlo simulation trials) of both Algorithm 1 (lines 4 through 7) and Algorithm 2 (lines 6 through 8) in Fig. 8a and 8b, respectively, where the RIS-UE distance is set to 2 m and the UE's velocity is set to 1 m/s. Convergence is considered to be accomplished if the evolution of the respective objective functions (16) and (8) is smaller than an arbitrarily chosen threshold $\epsilon \approx 10^{-15}$. Fig. 8a shows that (16) converges in just 3 iterations whereas Fig. 8a

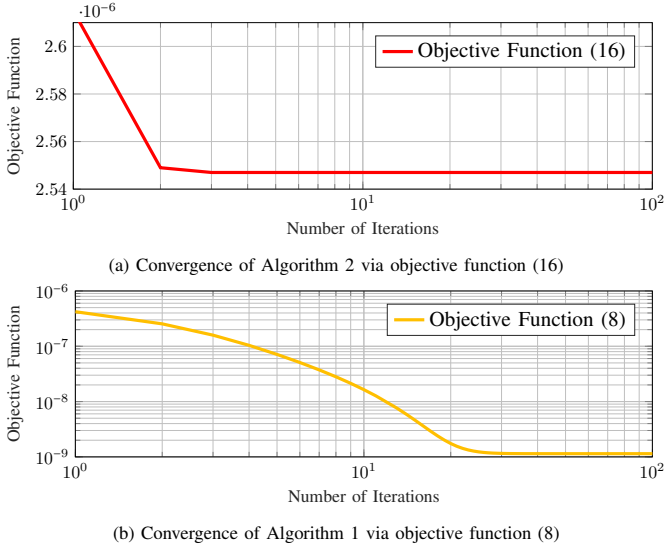


Fig. 8: Convergence rate of Algorithms 1 and 2, via objective functions (8) and (16) respectively, as a function of the number of iterations at $\rho = 2$ m RIS-UE distance and $v = 1$ m/s UE's velocity.

shows that (8) takes around 20 iterations to finally converge, which is still acceptable from an algorithmic point-of-view. This practically shows how quick the two algorithmic steps can be in a typical application case.

V. CONCLUSION

In this work, we have proposed a single-BS DL single-input-single-output (SISO) positioning scenario, by considering the 6D state estimation of a mobile UE, while relying on one reflective RIS in the presence of LoS blockage. We have accounted for small-scale velocity effects by modeling the RIS response in geometric NF (i.e., taking into account extra phase shifts at the RIS elements); and we have derived both theoretical position and velocity error bounds to be used as performance benchmarks. Then, we have designed a 6D estimation algorithm consisting of three subroutines. First, we assume the UE to be static and we coarsely estimate the position parameters via grid search which are then passed to an iterative subroutine that refines the results while assuming the knowledge of the UE's velocity. Then, we estimate the velocity parameters with the perfect knowledge assumption of the UE's position. We have introduced algorithmic time complexity analysis and we have simulated our algorithms against different system parameters, including the RIS-UE distance and UE's velocity. The obtained results show that our final algorithmic results attain the theoretical performance bounds at close RIS-UE distances. For farther distances however, as our CF refinement routines are shown to experience much poorer performance, we have resolved this issue by introducing a global refinement process (as part of our algorithm), which restores a fine performance level. Furthermore, we have tested the resilience of our algorithm against both low SNR values and multipath interference.

This work is to be extended in multiple dimensions, including the integration of UE state tracking process with the help of Bayesian filters. Moreover, previous research works could

be leveraged to include location-based RIS phase optimization routines as well as realistic RIS hardware prototypes.

APPENDIX A DERIVATION OF $f_{\ell,m}(\mathbf{p}, \mathbf{v})$ IN (4)

Let's define the new UE position $\mathbf{p}_\ell = \mathbf{p} + \mathbf{\Delta}_\ell$ after a displacement by a vector $\mathbf{\Delta}_\ell = \mathbf{v}\ell T_s$. We also introduce $\mathbf{p}_m - \mathbf{p} = \mathbf{\delta}_m$. Accordingly, one can write

$$\|\mathbf{p}_m - \mathbf{p}_\ell\| = \|\mathbf{\delta}_m\| \frac{\|\mathbf{\delta}_m - \mathbf{\Delta}_\ell\|}{\|\mathbf{\delta}_m\|}, \quad (40)$$

$$= \|\mathbf{\delta}_m\| \sqrt{\frac{(\mathbf{\delta}_m - \mathbf{\Delta}_\ell)^\top (\mathbf{\delta}_m - \mathbf{\Delta}_\ell)}{\|\mathbf{\delta}_m\|^2}}, \quad (41)$$

$$= \|\mathbf{\delta}_m\| \sqrt{1 - \frac{2\mathbf{\delta}_m^\top \mathbf{\Delta}_\ell}{\|\mathbf{\delta}_m\|^2} + \frac{\|\mathbf{\Delta}_\ell\|^2}{\|\mathbf{\delta}_m\|^2}}. \quad (42)$$

When the total displacement of the UE during the entire observation interval is negligible compared to the distance between the RIS and the UE, i.e.,

$$\|\mathbf{v}\| \ll \frac{\max_m \|\mathbf{p}_m - \mathbf{p}\|}{LT_s}, \quad (43)$$

the last term under the square root in (42) can be neglected. Under the same condition (43), the second term under the square root in (42) is much smaller than 1, which allows us to apply the first-order Taylor series approximation $\sqrt{1 - 2x} \approx 1 - x$ for $x \ll 1$. Combined, this allows us to rewrite (42) as

$$\begin{aligned} \|\mathbf{p}_m - \mathbf{p}_\ell\| &\approx \|\mathbf{\delta}_m\| - \frac{\mathbf{\delta}_m^\top \mathbf{\Delta}_\ell}{\|\mathbf{\delta}_m\|}, \\ &= \|\mathbf{p}_m - \mathbf{p}\| - \frac{(\mathbf{p}_m - \mathbf{p})^\top}{\|\mathbf{p}_m - \mathbf{p}\|} \mathbf{v}\ell T_s, \\ &= d_m - \mathbf{u}_m^\top(\mathbf{p}) \mathbf{v}\ell T_s. \end{aligned} \quad (44)$$

APPENDIX B FF APPROXIMATION

The NF RIS response form in (2) can be in fact approximated to its equivalent FF form as following.

From the geometry of Fig. 1 we have:

$$d_m = \sqrt{d_r^2 + q_m^2 - 2d_r q_m \kappa}, \quad (45)$$

where $q_m = \|\mathbf{p}_m - \mathbf{p}_r\|$ and $\kappa \triangleq \sin(\phi) \cos(\theta - \psi_m)$ is the constant holding the angular (azimuth and elevation) terms. Using first-order Taylor's expansion, the function $f(x) = \sqrt{1 + x^2 - 2x\kappa}$ can be approximated around $x = 0$ into $f(x) \approx 1 - x\kappa$; then given that the RIS is large enough and the UE is far from the surface, d_m can be approximated as:

$$d_m \approx d_r \left(1 - \frac{q_m}{d_r} \kappa\right) \quad (46)$$

$$= d_r - q_m \kappa, \quad (47)$$

then

$$\|\mathbf{p}_m - \mathbf{p}\| - \|\mathbf{p}_r - \mathbf{p}\| = d_m - d_r = -q_m \sin(\phi) \cos(\theta - \psi_m). \quad (48)$$

Following [35], we then approximate the steering vector in far-field as

$$[\mathbf{a}(\theta, \phi)]_m \approx \exp(-j(\mathbf{p}_m - \mathbf{p}_r)^\top \mathbf{k}(\phi, \theta)), \quad (49)$$

where $\mathbf{k}(\phi, \theta) = -\frac{2\pi}{\lambda} [\sin \phi \cos \theta, \sin \phi \sin \theta, \cos \phi]^\top$

APPENDIX C GRADIENT OF $f_{\ell, m}(\mathbf{p}, \mathbf{v})$

In the linearized RIS response model from (18), we have that

$$\begin{aligned} \nabla_{\mathbf{p}} f_{\ell, m}(\mathbf{p}, \mathbf{v}) &= \frac{\mathbf{p}_m - \mathbf{p}}{d_m} - \frac{\mathbf{p}_r - \mathbf{p}}{d_r} \\ &+ \left(\frac{\partial \mathbf{u}_m(\mathbf{p})}{\partial \mathbf{p}} - \frac{\partial \mathbf{u}_r(\mathbf{p})}{\partial \mathbf{p}} \right)^\top \mathbf{v} \ell T_s \\ &= \mathbf{u}_m(\mathbf{p}) - \mathbf{u}_r(\mathbf{p}) + \nabla_{\mathbf{p}}^\top \gamma_m \mathbf{v} \ell T_s \in \mathbb{R}^{3 \times 1}, \quad (50) \\ \nabla_{\mathbf{p}} \gamma_m &\triangleq \left(\frac{\|\mathbf{p}_m - \mathbf{p}\|^2 \mathbf{1}_{3 \times 3} - (\mathbf{p}_m - \mathbf{p})(\mathbf{p}_m - \mathbf{p})^\top}{\|\mathbf{p}_m - \mathbf{p}\|^3} \right. \\ &\quad \left. - \frac{\|\mathbf{p}_r - \mathbf{p}\|^2 \mathbf{1}_{3 \times 3} - (\mathbf{p}_r - \mathbf{p})(\mathbf{p}_r - \mathbf{p})^\top}{\|\mathbf{p}_r - \mathbf{p}\|^3} \right) \in \mathbb{R}^{3 \times 3}. \quad (51) \end{aligned}$$

APPENDIX D DERIVATION OF \mathbf{p}_δ

The problem (27) for fixed $\alpha = \widehat{\alpha}$ can be reduced to

$$\widehat{\mathbf{p}}_\delta = \arg \min_{\mathbf{p}_\delta \in \mathbb{R}^{3 \times 1}} \|\mathbf{y} - \widehat{\alpha}(\boldsymbol{\eta} + j\boldsymbol{\Xi}^\top \mathbf{p}_\delta)\|^2. \quad (52)$$

Opening up the terms in (52), we have

$$\begin{aligned} \mathcal{L}(\mathbf{p}_\delta) &\triangleq \|\mathbf{y} - \widehat{\alpha}(\boldsymbol{\eta} + j\boldsymbol{\Xi}^\top \mathbf{p}_\delta)\|^2, \\ &= \|\mathbf{y}\|^2 - 2 \operatorname{Re} \{ \mathbf{y}^H \widehat{\alpha}(\boldsymbol{\eta} + j\boldsymbol{\Xi}^\top \mathbf{p}_\delta) \} + |\widehat{\alpha}|^2 \|\boldsymbol{\eta} + j\boldsymbol{\Xi}^\top \mathbf{p}_\delta\|^2, \\ &= \|\mathbf{y}\|^2 - 2 \operatorname{Re} \{ \widehat{\alpha} \mathbf{y}^H \boldsymbol{\eta} \} - 2 \operatorname{Re} \{ j\widehat{\alpha} \mathbf{y}^H \boldsymbol{\Xi}^\top \mathbf{p}_\delta \} + |\widehat{\alpha}|^2 \|\boldsymbol{\eta}\|^2 \\ &\quad + 2|\widehat{\alpha}|^2 \operatorname{Re} \{ j\boldsymbol{\eta}^H \boldsymbol{\Xi}^\top \mathbf{p}_\delta \} + |\widehat{\alpha}|^2 \|j\boldsymbol{\Xi}^\top \mathbf{p}_\delta\|^2, \\ &= |\widehat{\alpha}|^2 \mathbf{p}_\delta^\top \boldsymbol{\Xi}^* \boldsymbol{\Xi}^\top \mathbf{p}_\delta + (2|\widehat{\alpha}|^2 \operatorname{Re} \{ j\boldsymbol{\eta}^H \boldsymbol{\Xi}^\top \} \\ &\quad - 2 \operatorname{Re} \{ j\widehat{\alpha} \mathbf{y}^H \boldsymbol{\Xi}^\top \}) \mathbf{p}_\delta + \|\mathbf{y}\|^2 \\ &\quad - 2 \operatorname{Re} \{ \widehat{\alpha} \mathbf{y}^H \boldsymbol{\eta} \} + |\widehat{\alpha}|^2 \|\boldsymbol{\eta}\|^2, \quad (53) \end{aligned}$$

where we have used the fact that \mathbf{p}_δ is a real vector. According to Lemma S1 in the supplementary material of [42], $\mathbf{p}_\delta^\top \boldsymbol{\Xi}^* \boldsymbol{\Xi}^\top \mathbf{p}_\delta = \mathbf{p}_\delta^\top \operatorname{Re} \{ \boldsymbol{\Xi}^* \boldsymbol{\Xi}^\top \} \mathbf{p}_\delta$ since $\mathbf{p}_\delta \in \mathbb{R}^{3 \times 1}$ and $\boldsymbol{\Xi}^* \boldsymbol{\Xi}^\top$ is Hermitian. Then, ignoring the constant terms in (53), the problem (52) can be re-written as

$$\widehat{\mathbf{p}}_\delta = \arg \min_{\mathbf{p}_\delta \in \mathbb{R}^{3 \times 1}} \{ |\widehat{\alpha}|^2 \mathbf{p}_\delta^\top \operatorname{Re} \{ \boldsymbol{\Xi}^* \boldsymbol{\Xi}^\top \} \mathbf{p}_\delta \quad (54)$$

$$+ (2|\widehat{\alpha}|^2 \operatorname{Re} \{ j\boldsymbol{\eta}^H \boldsymbol{\Xi}^\top \} - 2 \operatorname{Re} \{ j\widehat{\alpha} \mathbf{y}^H \boldsymbol{\Xi}^\top \}) \mathbf{p}_\delta \}. \quad (55)$$

Since (55) is an unconstrained quadratic optimization problem, the solution can readily be obtained in closed-form as

$$\widehat{\mathbf{p}}_\delta = \frac{1}{|\widehat{\alpha}|^2} (\operatorname{Re} \{ \boldsymbol{\Xi}^* \boldsymbol{\Xi}^\top \})^{-1} \operatorname{Im} \{ \boldsymbol{\Xi} (|\widehat{\alpha}|^2 \boldsymbol{\eta}^* - \widehat{\alpha} \mathbf{y}^*) \}. \quad (56)$$

Notice that the 3×3 matrix

$$\operatorname{Re} \{ \boldsymbol{\Xi}^* \boldsymbol{\Xi}^\top \} = \sum_{\ell=1}^L \operatorname{Re} \{ \boldsymbol{\xi}_\ell^* \boldsymbol{\xi}_\ell^\top \} \quad (57)$$

is full-rank for $L \geq 3$ under mild conditions (e.g., if RIS phase profiles are random). Hence, if the number of transmissions is at least 3, then the closed-form UE position can be computed using (28).

Update α for fixed \mathbf{p}_δ : The solution of α for a fixed $\mathbf{p}_\delta = \widehat{\mathbf{p}}_\delta$ is given by

$$\widehat{\alpha} = \frac{(\boldsymbol{\eta} + j\boldsymbol{\Xi}^\top \widehat{\mathbf{p}}_\delta)^H \mathbf{y}}{\|\boldsymbol{\eta} + j\boldsymbol{\Xi}^\top \widehat{\mathbf{p}}_\delta\|^2}. \quad (58)$$

REFERENCES

- [1] A. Shahraki, M. Abbasi, M. J. Piran, M. Chen, and S. Cui, "A Comprehensive Survey on 6G Networks: Applications, Core Services, Enabling Technologies, and Future Challenges," *ArXiv*, vol. abs/2101.12475, 2021. [Online]. Available: <https://api.semanticscholar.org/CorpusID:231728460>
- [2] C.-X. Wang, X. You, X. Gao, X. Zhu, Z. Li, C. Zhang, H. Wang, Y. Huang, Y. Chen, H. Haas, J. S. Thompson, E. G. Larsson, M. D. Renzo, W. Tong, P. Zhu, X. Shen, H. V. Poor, and L. Hanzo, "On the Road to 6G: Visions, Requirements, Key Technologies, and Testbeds," *IEEE Communications Surveys & Tutorials*, vol. 25, no. 2, pp. 905–974, 2023.
- [3] H. Tataria, M. Shafi, A. F. Molisch, M. Dohler, H. Sjöland, and F. Tufvesson, "6G Wireless Systems: Vision, Requirements, Challenges, Insights, and Opportunities," *Proceedings of the IEEE*, vol. 109, no. 7, pp. 1166–1199, 2021.
- [4] B. Ji, Y. Han, S. Liu, F. Tao, G. Zhang, Z. Fu, and C. Li, "Several Key Technologies for 6G: Challenges and Opportunities," *IEEE Communications Standards Magazine*, vol. 5, no. 2, pp. 44–51, 2021.
- [5] L. Bariah, L. Mohjazi, S. Muhaidat, P. C. Sofotasios, G. K. Kurt, H. Yanikomeroglu, and O. A. Dobre, "A Prospective Look: Key Enabling Technologies, Applications and Open Research Topics in 6G Networks," *IEEE Access*, vol. 8, pp. 174 792–174 820, 2020.
- [6] S. Chen, Y.-C. Liang, S. Sun, S. Kang, W. Cheng, and M. Peng, "Vision, requirements, and technology trend of 6g: How to tackle the challenges of system coverage, capacity, user data-rate and movement speed," *IEEE Wireless Communications*, vol. 27, no. 2, pp. 218–228, 2020.
- [7] F. Tariq, M. R. A. Khandaker, K.-K. Wong, M. A. Imran, M. Bennis, and M. Debbah, "A Speculative Study on 6G," *IEEE Wireless Communications*, vol. 27, no. 4, pp. 118–125, 2020.
- [8] J. Zhao, "A Survey of Intelligent Reflecting Surfaces (IRSs): Towards 6G Wireless Communication Networks with Massive MIMO 2.0," 2019. [Online]. Available: <https://api.semanticscholar.org/CorpusID:208088173>
- [9] M. Di Renzo, A. Zappone, M. Debbah, M.-S. Alouini, C. Yuen, J. de Rosny, and S. Tretyakov, "Smart Radio Environments Empowered by Reconfigurable Intelligent Surfaces: How it Works, State of Research, and the Road Ahead," *IEEE Journal on Selected Areas in Communications*, vol. 38, no. 11, pp. 2450–2525, 2020.
- [10] E. C. Strinati, G. C. Alexandropoulos, H. Wymeersch, B. Denis, V. Sciancalepore, R. D'Errico, A. Clemente, D.-T. Phan-Huy, E. De Carvalho, and P. Popovski, "Reconfigurable, Intelligent, and Sustainable Wireless Environments for 6G Smart Connectivity," *IEEE Communications Magazine*, vol. 59, no. 10, pp. 99–105, 2021.
- [11] Y. Liu, X. Liu, X. Mu, T. Hou, J. Xu, M. Di Renzo, and N. Al-Dhahir, "Reconfigurable Intelligent Surfaces: Principles and Opportunities," *IEEE Communications Surveys & Tutorials*, vol. 23, no. 3, pp. 1546–1577, 2021.
- [12] O. Özdoğan, E. Björnson, and E. G. Larsson, "Intelligent Reflecting Surfaces: Physics, Propagation, and Pathloss Modeling," *IEEE Wireless Communications Letters*, vol. 9, no. 5, pp. 581–585, 2020.
- [13] Q. Wu and R. Zhang, "Towards Smart and Reconfigurable Environment: Intelligent Reflecting Surface Aided Wireless Network," *IEEE Communications Magazine*, vol. 58, no. 1, pp. 106–112, 2020.
- [14] E. Basar, M. Di Renzo, J. De Rosny, M. Debbah, M.-S. Alouini, and R. Zhang, "Wireless Communications Through Reconfigurable Intelligent Surfaces," *IEEE Access*, vol. 7, pp. 116 753–116 773, 2019.
- [15] G. C. Alexandropoulos, G. Leroosey, M. Debbah, and M. Fink, "Reconfigurable Intelligent Surfaces and Metamaterials: The Potential of Wave Propagation Control for 6G Wireless Communications," 2020. [Online]. Available: <https://arxiv.org/abs/2006.11136>

- [16] C. Huang, A. Zappone, G. C. Alexandropoulos, M. Debbah, and C. Yuen, "Reconfigurable Intelligent Surfaces for Energy Efficiency in Wireless Communication," *IEEE Trans. Wireless Commun.*, vol. 18, no. 8, pp. 4157–4170, Aug. 2019.
- [17] Q. Wu and R. Zhang, "Intelligent Reflecting Surface Enhanced Wireless Network via Joint Active and Passive Beamforming," *IEEE Trans. Wireless Commun.*, vol. 18, no. 11, pp. 5394–5409, Nov. 2019.
- [18] H. Wymeersch, J. He, B. Denis, A. Clemente, and M. Juntti, "Radio Localization and Mapping With Reconfigurable Intelligent Surfaces: Challenges, Opportunities, and Research Directions," *IEEE Vehicular Technology Magazine*, vol. 15, no. 4, pp. 52–61, 2020.
- [19] F. Zafari, A. Gkelias, and K. K. Leung, "A Survey of Indoor Localization Systems and Technologies," *IEEE Communications Surveys & Tutorials*, vol. 21, no. 3, pp. 2568–2599, 2019.
- [20] A. Bourdoux, A. noll Barreto, B. van Liempd, C. Lima, D. Dardari, D. Belot, E.-S. Lohan, G. Seco-Granados, H. Sarrieddeen, H. Wymeersch, J. Suutala, J. Saloranta, M. Guillaud, M. Isomursu, M. Valkama, M. R. K. Aziz, R. Berkvens, T. Sanguanpuak, T. Svensson, and Y. Miao, "6G White Paper on Localization and Sensing," *ArXiv*, vol. abs/2006.01779, 2020. [Online]. Available: <https://api.semanticscholar.org/CorpusID:219179573>
- [21] M. Rahal, B. Denis, K. Keykhosravi, B. Uguen, and H. Wymeersch, "RIS-Enabled Localization Continuity Under Near-Field Conditions," in *IEEE International Workshop on Signal Processing Advances in Wireless Communications (SPAWC)*, 2021, pp. 436–440.
- [22] K. Keykhosravi, B. Denis, G. C. Alexandropoulos, Z. S. He, A. Albanese, V. Sciancalepore, and H. Wymeersch, "Leveraging RIS-Enabled Smart Signal Propagation for Solving Infeasible Localization Problems: Scenarios, Key Research Directions, and Open Challenges," *IEEE Vehicular Technology Magazine*, vol. 18, no. 2, pp. 20–28, 2023.
- [23] H. Wymeersch and B. Denis, "Beyond 5G Wireless Localization with Reconfigurable Intelligent Surfaces," in *IEEE International Conference on Communications (ICC)*, Jun. 2020. [Online]. Available: <https://ieeexplore.ieee.org/document/9148744/>
- [24] A. Elzanaty, A. Guerra, F. Guidi, and M.-S. Alouini, "Reconfigurable Intelligent Surfaces for Localization: Position and Orientation Error Bounds," *IEEE Transactions on Signal Processing*, vol. 69, pp. 5386–5402, 2021.
- [25] J. He, H. Wymeersch, L. Kong, O. Silvén, and M. Juntti, "Large Intelligent Surface for Positioning in Millimeter Wave MIMO Systems," in *IEEE Vehicular Technology Conference (VTC)*, 2020.
- [26] H. Zhang, H. Zhang, B. Di, K. Bian, Z. Han, and L. Song, "Towards Ubiquitous Positioning by Leveraging Reconfigurable Intelligent Surface," *IEEE Communications Letters*, vol. 25, no. 1, pp. 284–288, 2021.
- [27] K. Keykhosravi, M. F. Keskin, G. Seco-Granados, and H. Wymeersch, "SISO RIS-enabled joint 3D downlink localization and synchronization," in *IEEE International Conference on Communications (ICC)*, 2021.
- [28] M. Rahal, B. Denis, K. Keykhosravi, M. F. Keskin, B. Uguen, and H. Wymeersch, "Constrained RIS Phase Profile Optimization and Time Sharing for Near-Field Localization," in *2022 IEEE 95th Vehicular Technology Conference: (VTC2022-Spring)*, 2022, pp. 1–6.
- [29] Y. Liu, E. Liu, R. Wang, and Y. Geng, "Reconfigurable intelligent surface aided wireless localization," in *IEEE International Conference on Communications (ICC)*, 2021.
- [30] K. Keykhosravi, M. F. Keskin, G. Seco-Granados, P. Popovski, and H. Wymeersch, "RIS-Enabled SISO Localization Under User Mobility and Spatial-Wideband Effects," *IEEE Journal of Selected Topics in Signal Processing*, vol. 16, no. 5, pp. 1125–1140, 2022.
- [31] L. Xie, X. Yu, and S. Song, "Intelligent Reflecting Surface-Aided Maneuvering Target Sensing: True Velocity Estimation," in *2022 International Symposium on Wireless Communication Systems (ISWCS)*, 2022, pp. 1–6.
- [32] A. Guerra, F. Guidi, D. Dardari, and P. M. Djurić, "3D Source Tracking with Large Antenna Arrays in the Fresnel Region," in *2021 IEEE 22nd International Workshop on Signal Processing Advances in Wireless Communications (SPAWC)*, 2021, pp. 426–430.
- [33] M. Ammous and S. Valaee, "Positioning and Tracking Using Reconfigurable Intelligent Surfaces and Extended Kalman Filter," in *2022 IEEE 95th Vehicular Technology Conference: (VTC2022-Spring)*, 2022, pp. 1–6.
- [34] S. Palmucci, A. Guerra, A. Abrardo, and D. Dardari, "Two-Timescale Joint Precoding Design and RIS Optimization for User Tracking in Near-Field MIMO Systems," *IEEE Transactions on Signal Processing*, pp. 1–16, 2023.
- [35] Z. Abu-Shaban, K. Keykhosravi, M. F. Keskin, G. C. Alexandropoulos, G. Seco-Granados, and H. Wymeersch, "Near-Field Localization with a Reconfigurable Intelligent Surface Acting as Lens," in *ICC 2021 - IEEE International Conference on Communications*, 2021, pp. 1–6.
- [36] D. Dardari, N. Decarli, A. Guerra, and F. Guidi, "LOS/NLOS near-field localization with a large reconfigurable intelligent surface," *IEEE Transactions on Wireless Communications*, vol. 21, no. 6, pp. 4282–4294, 2022.
- [37] A. Abrardo, D. Dardari, and M. Di Renzo, "Intelligent Reflecting Surfaces: Sum-Rate Optimization Based on Statistical Position Information," *IEEE Transactions on Communications*, vol. 69, no. 10, pp. 7121–7136, 2021.
- [38] F. Jiang, A. Abrardo, K. Keykhosravi, H. Wymeersch, D. Dardari, and M. Di Renzo, "Two-Timescale Transmission Design and ris optimization for integrated localization and communications," *IEEE Transactions on Wireless Communications*, pp. 1–1, 2023.
- [39] K. Zhi, C. Pan, H. Ren, and K. Wang, "Power Scaling Law Analysis and Phase Shift Optimization of RIS-Aided Massive MIMO Systems With Statistical CSI," *IEEE Transactions on Communications*, vol. 70, no. 5, pp. 3558–3574, 2022.
- [40] Z. Peng, T. Li, C. Pan, H. Ren, and J. Wang, "RIS-Aided D2D Communications Relying on Statistical CSI With Imperfect Hardware," *IEEE Communications Letters*, vol. 26, no. 2, pp. 473–477, 2022.
- [41] N. Iqbal, J. Luo, R. Müller, G. Steinböck, C. Schneider, D. A. Dupleich, S. Häfner, and R. S. Thomä, "Multipath Cluster Fading Statistics and Modeling in Millimeter-Wave Radio Channels," *IEEE Transactions on Antennas and Propagation*, vol. 67, no. 4, pp. 2622–2632, 2019.
- [42] M. F. Keskin, H. Wymeersch, and V. Koivunen, "Monostatic sensing with OFDM under phase noise: From mitigation to exploitation," *IEEE Transactions on Signal Processing*, vol. 71, pp. 1363–1378, 2023.